nature portfolio

https://doi.org/10.1038/s41558-022-01403-8

Supplementary information

Widespread shift from ecosystem energy to water limitation with climate change

In the format provided by the authors and unedited

Supplementary material

Figures

All figures are created with the ggplot2 package and, if applicable, the country borders using the maptools package[1,2].

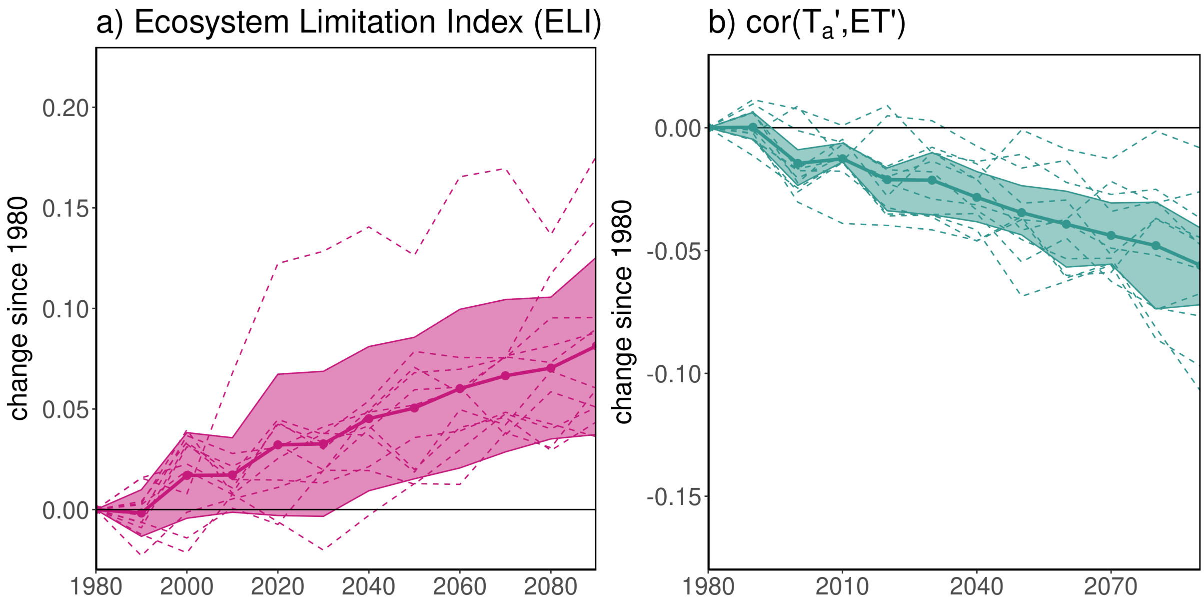

Supplementary figure 1: a) Past and projected global trends in ELI based on air temperature anomalies and b) cor(T_a′,ET′). Dashed colored lines depict the globally and decadally average time series of all respective variables per individual model. Solid lines with dots depict multi-model mean time series inferred from the model-specific time series, where the shaded regions cover +/- 1 multi-model standard deviation. The y-axis denotes the change since 1980 in respective units. Global averages are calculated over land grid cells that have complete time series for all models and variables and are weighted according to the surface area per grid cell.

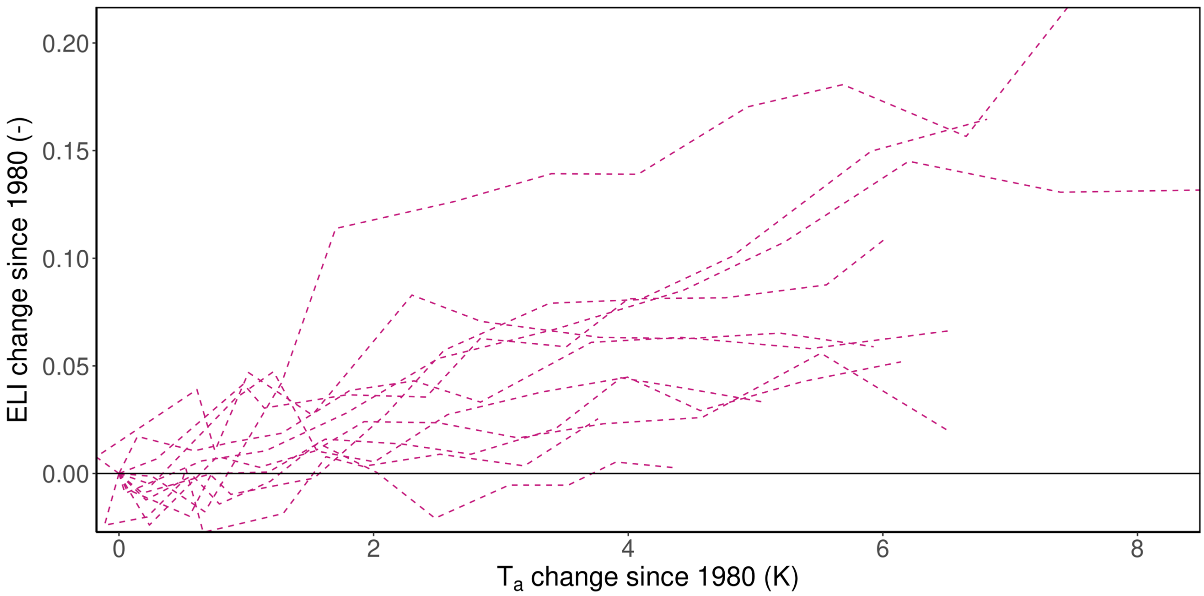

Supplementary Figure 2: Past and projected global trends in ELI for model-specific air temperature warming levels. Dashed colored lines depict the globally and decadally average time series of ELI per individual model.

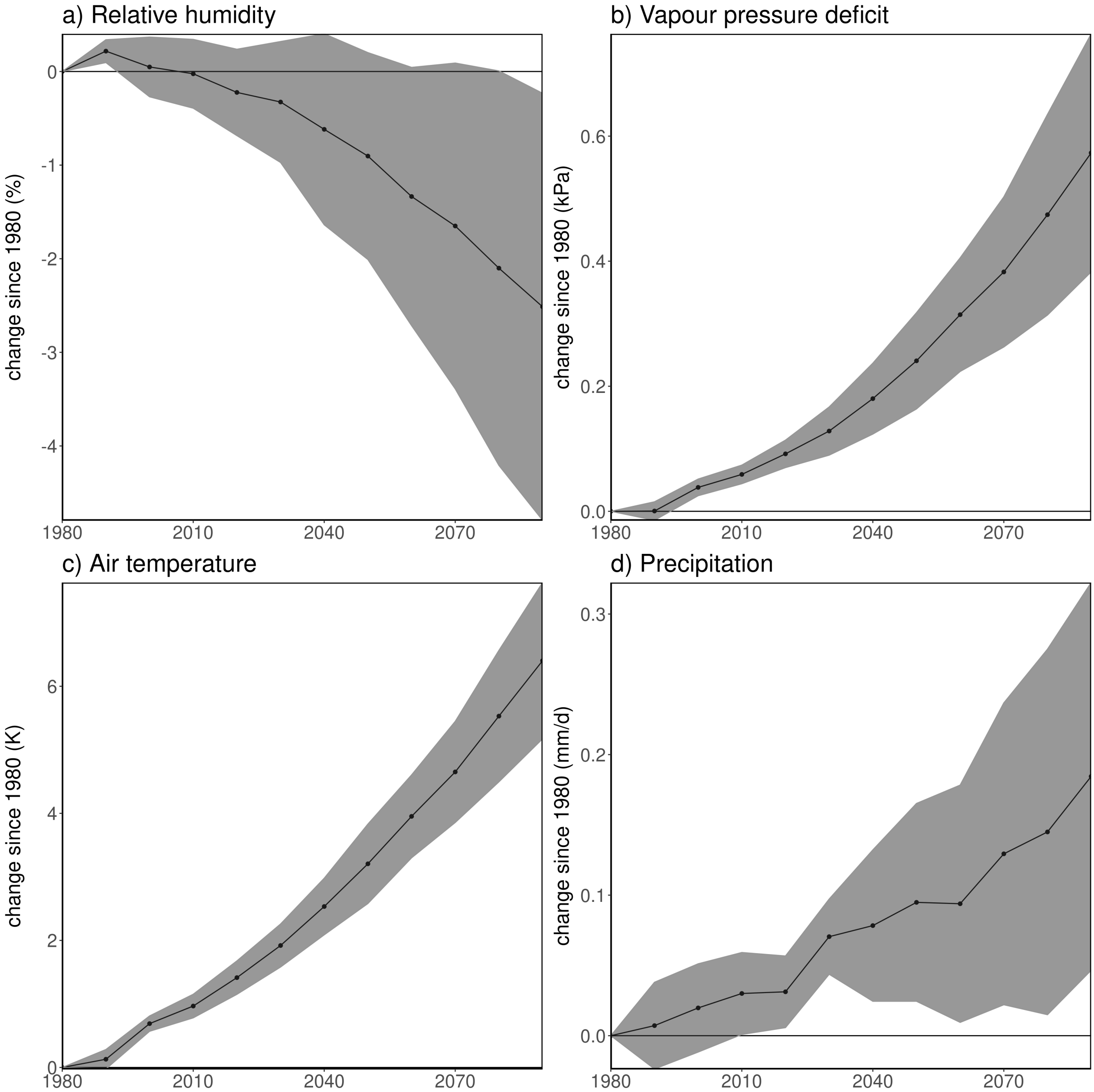

Supplementary figure 3: Past and projected global climate trends. Global trends of a) relative humidity, b) vapour pressure deficit, c) air temperature and d) precipitation from 1980 - 2100 for 7 models only (Methods). Solid lines with dots depict the multi-model mean time series of the respective variables inferred from model-specific globally and decadally averaged time series, where the shaded regions cover +/- 1 multi-model standard deviation. The y-axis denotes the change since 1980 in respective units. Global averages are calculated over land grid cells that have complete time series for all models and variables and are weighted according to the surface area per grid cell.

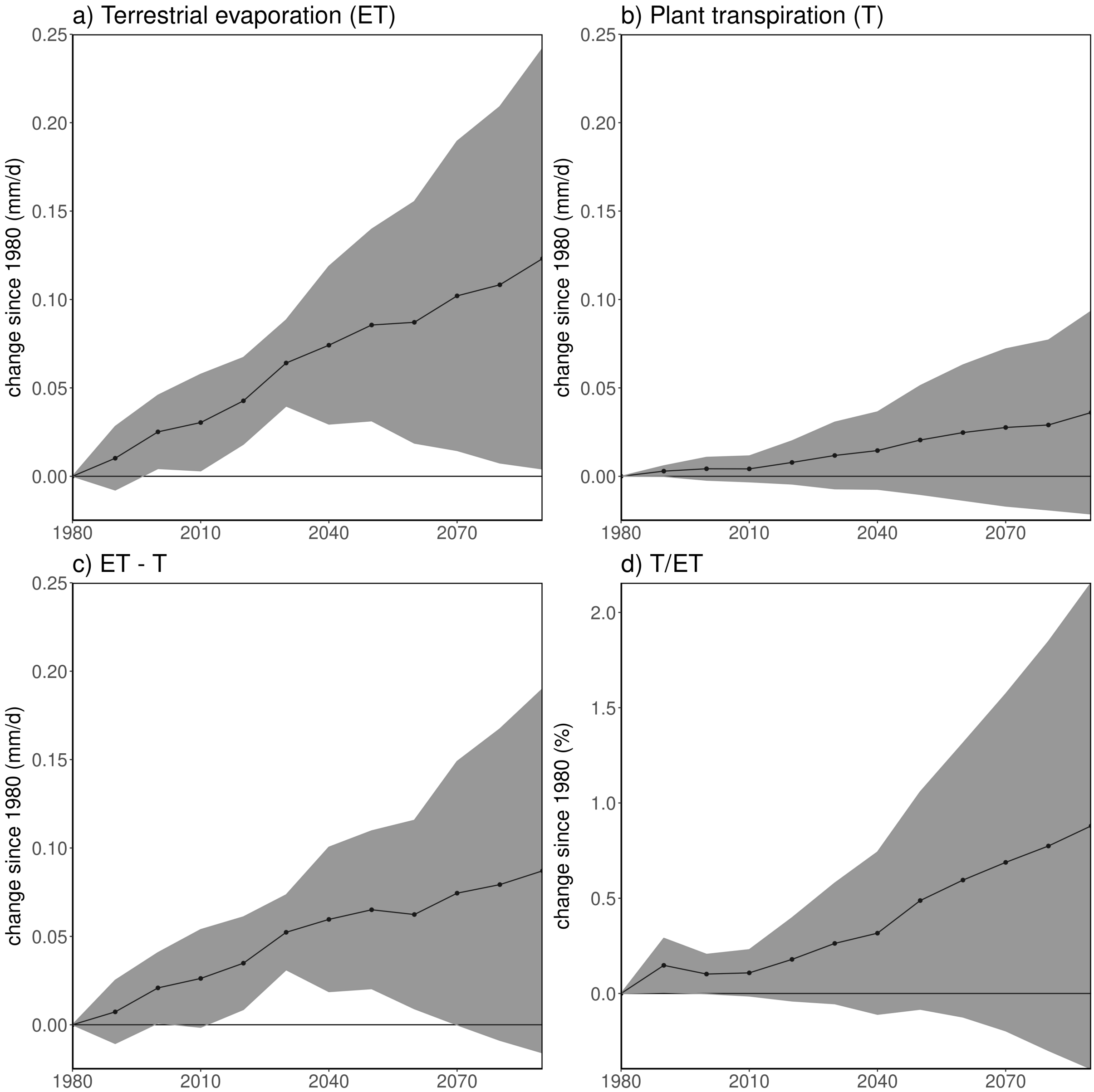

Supplementary figure 4: Past and projected global trends of evaporative components. Global trends of a) terrestrial evaporation, b) plant transpiration (Methods), c) ET – T, effectively the sum of bare soil evaporation and canopy interception, d) fraction plant transpired water (plant transpiration over terrestrial evaporation) from 1980 - 2100 for 7 models only (Methods). Solid lines with dots depict the multi-model mean time series of the respective variables inferred from model-specific globally and decadally averaged time series, where the shaded regions cover +/- 1 multi-model standard deviation. The y-axis denotes the change since

1980 in respective units. Global averages are calculated over land grid cells that have complete time series for all models and variables and are weighted according to the surface area per grid cell.

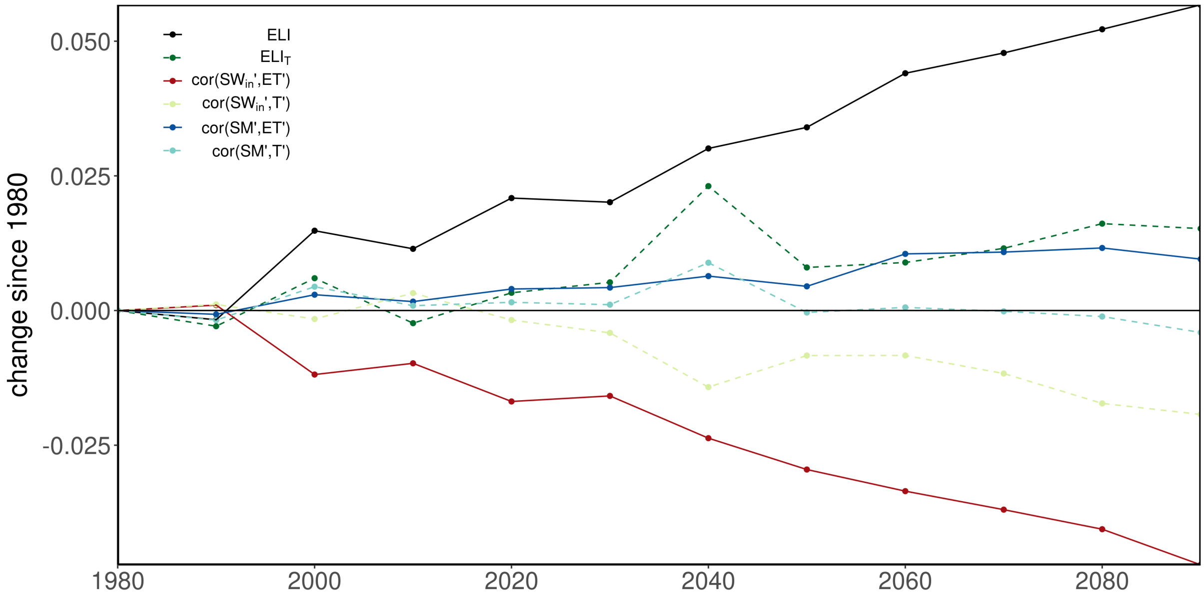

Supplementary figure 5: Global trends of Ecosystem Water Limitation Index and its individual components with terrestrial evaporation and transpiration for 7 models only (Methods). Individual components consist of the correlation between anomalies of either incoming shortwave radiation (SW_{in}) or soil moisture (SM) with either terrestrial evaporation (solid lines) or transpiration (dashed lines). Global averages are calculated over land grid cells that have complete time series for all models and variables and are weighted according to the surface area per grid cell. Solid and dashed lines with dots depict the multi-model mean time series of the variables displayed in the legend inferred from model-specific globally and decadally averaged time series, where the shaded regions cover +/- 1 multi-model standard deviation. All y-axes denote changes since 1980.

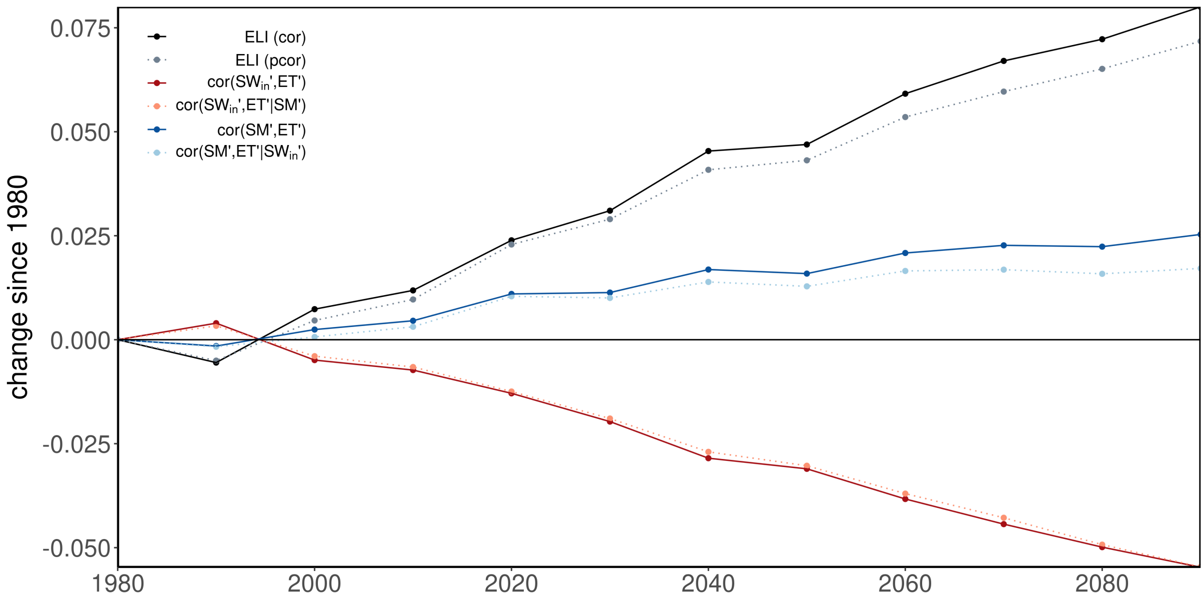

Supplementary figure 6: Confounding effects of energy on water control and vice versa on the Ecosystem Water Limitation Index and its individual components. Solid and dotted lines with dots depict the multi-model mean time series of the variables displayed in the legend inferred from model-specific globally and decadally averaged time series, where the shaded regions cover +/- 1 multi-model standard deviation. Global averages are calculated over land grid cells that have complete time series for all models and variables and are weighted according to the surface area per grid cell. Solid lines with dots are the ELI from Figure 1a) (black) and components (red, blue), where the dotted lines with dots are the ELI based on partial correlations. All y-axes denote changes since 1980.

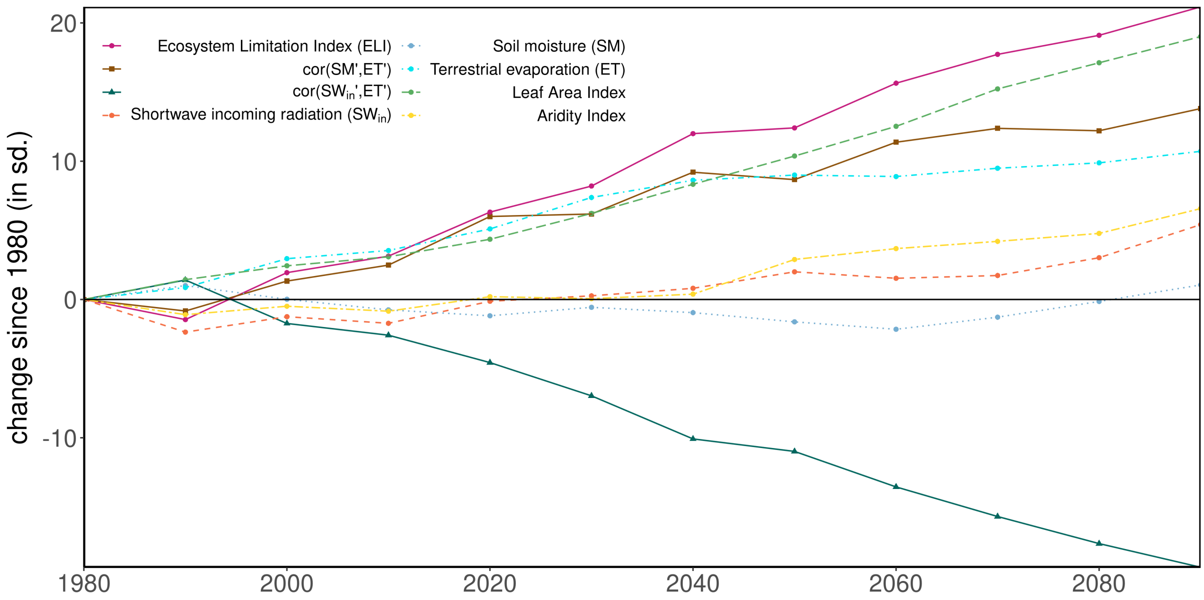

Supplementary figure 7: Past and projected global climate and vegetation trends normalized by natural variability (standard deviation of respective detrended decadal time series per variable; solid dotted lines). Solid lines with dots denote ELI and its individual components, the other line types denote other variables displayed in the legend. All lines with dots depict the multi-model mean time series of the variables displayed in the legend inferred from model-specific globally and decadally averaged time series. The y-axis denotes the change since 1980 in standard deviations (sd). Global averages are calculated over land grid cells that have complete time series for all models and variables and are weighted according to the surface area per grid cell.

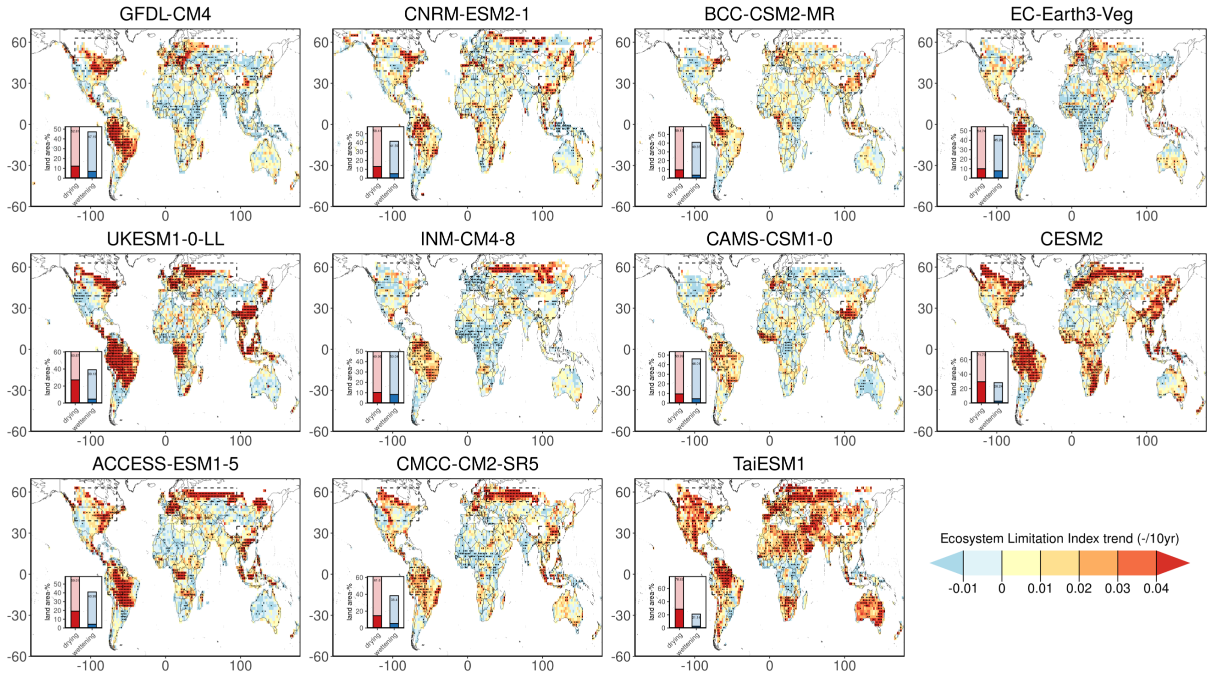

Supplementary figure 8: Ecosystem Water Limitation Index trends calculated per individual model. The trend in the multi-model mean time series of ELI (dots indicate significance: $p < 0.05$) is based on Kendall's tau statistic. The dashed boxes indicate regions of interest. The inset displays the fraction of the warm land area that is drying or wettening according to ELI trends.

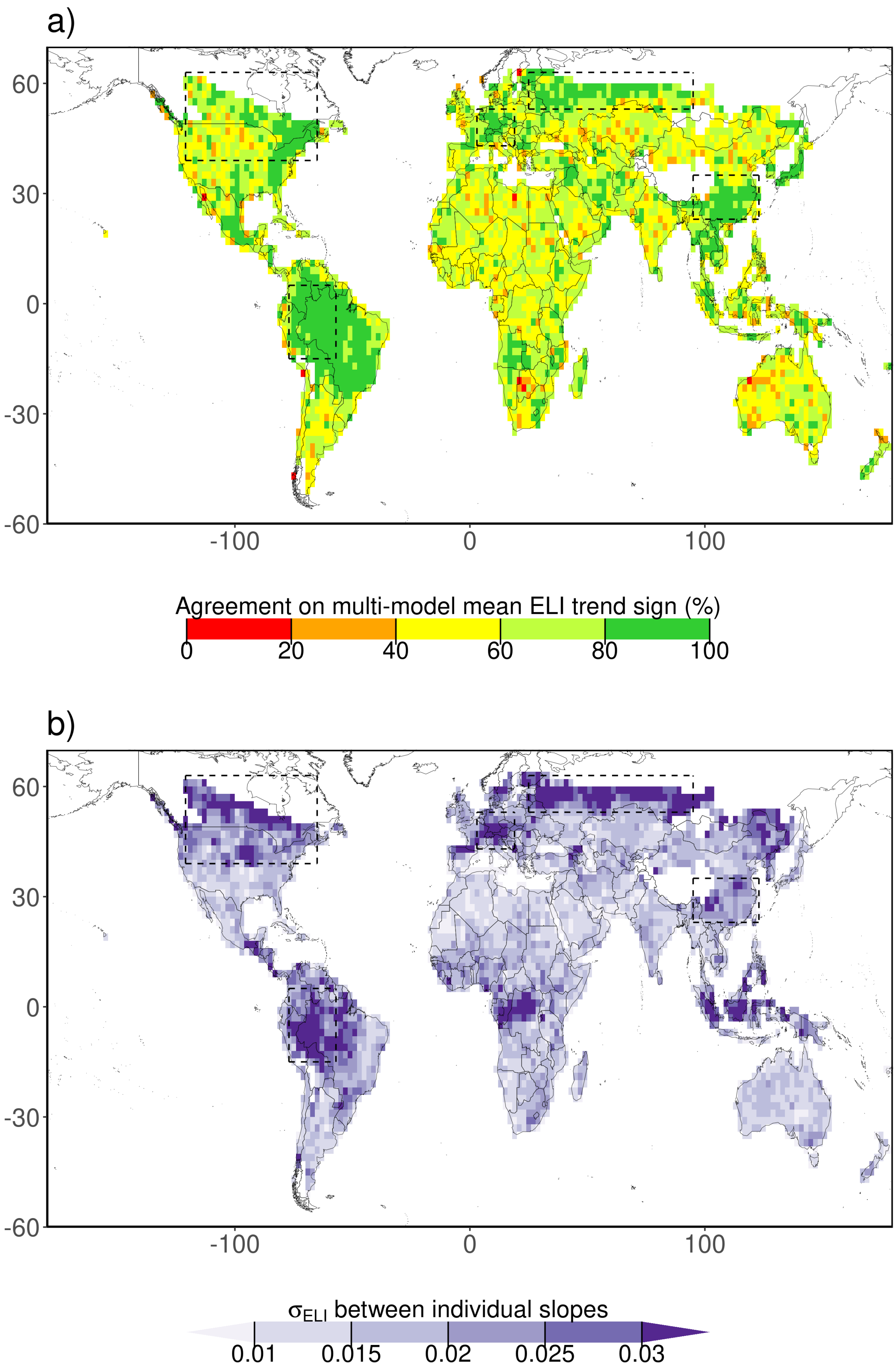
a)
60
30
0
-30
-60
-100
0
100
Agreement on multi-model mean ELI trend sign (%)
0
20
40
60
80
100
b)
60
30
0
-30
-60
-100
0
100
σELI between individual slopes
0.01
0.015
0.02
0.025
0.03

Supplementary figure 9: Comparison between trends of individual CMIP6 models from 1980 - 2100 (Supplementary figure 5). a) The percentage of models (from models that actually have a value in the respective grid cell) for which their respective ELI trends agree with the sign of the multi-model mean (Figure 2a). b) The standard deviation (σ_{ELI}) between individual slopes of CMIP6 models (Supplementary figure 4).

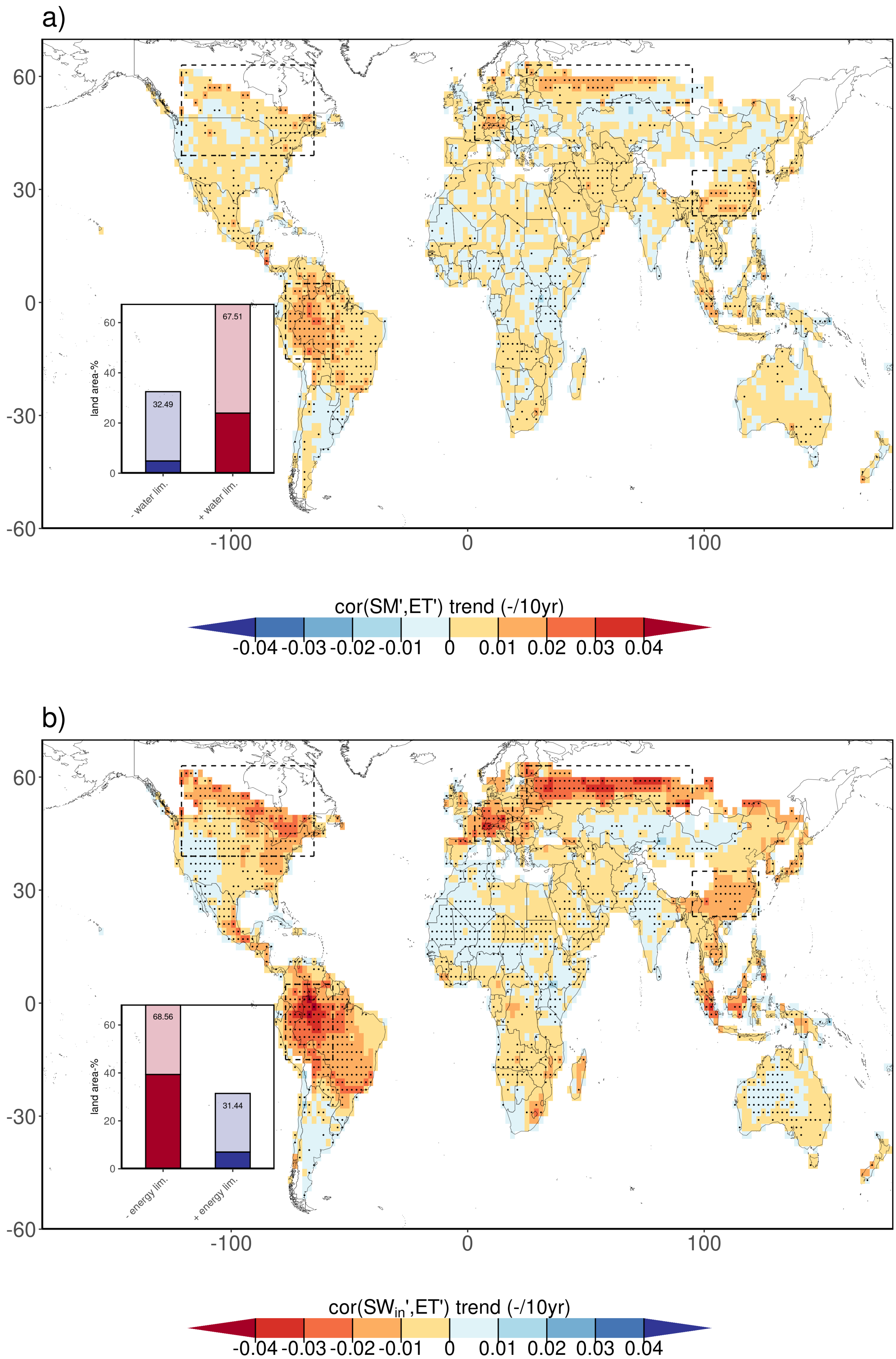
a)
60
30
0
-30
-60
-100
0
100
land area-%
60
40
20
0
32.49
67.51
- water lim.
+ water lim.
cor(SM',ET') trend (-/10yr)
-0.04 -0.03 -0.02 -0.01 0 0.01 0.02 0.03 0.04
b)
68.56
31.44
- energy lim.
+ energy lim.
cor(SW_in',ET') trend (-/10yr)
-0.04 -0.03 -0.02 -0.01 0 0.01 0.02 0.03 0.04

Supplementary figure 10: Mapping of the trends of individual components of ELI, cor(SM′,ET′) (a) and cor(SW_{in}′,ET′) (b) from 1980 to 2100. The trends are based on Kendall's tau statistic (dots indicate significance: $p < 0.05$). The dashed boxes indicate regions of interest. Inset plots display the fraction of warm land area with a decrease or increase in energy or water control ($p < 0.05$ is hued darker).

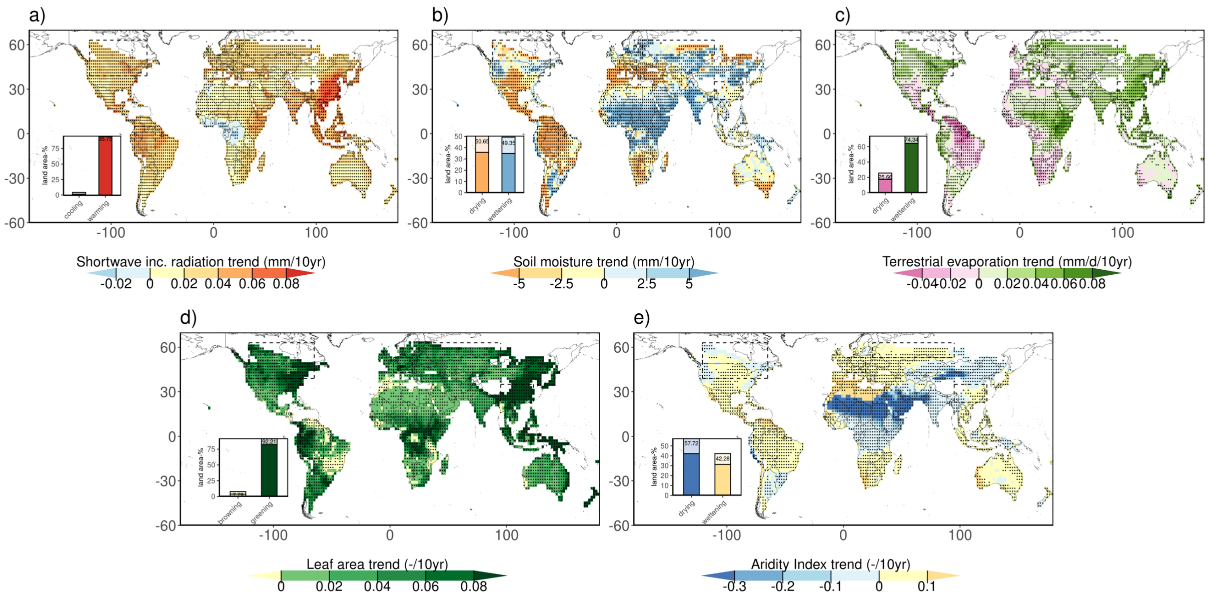

Supplementary figure 11: Trends based on multi-model mean time series of land-atmosphere variables from 1980 to 2100. The trends are based on Kendall's tau statistic (dots indicate significance: $p < 0.05$). The dashed boxes indicate regions of interest. Inset plots display the fraction of warm land area with negative or positive trends of all respective variables ($p < 0.05$ is hued darker).

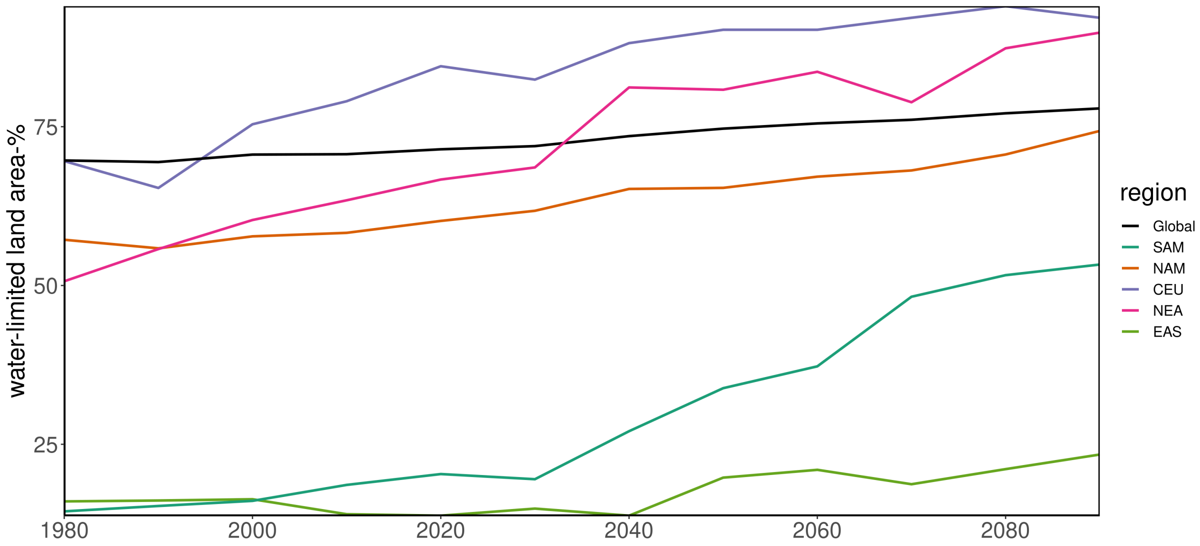

Supplementary Figure 12: Trends in water-limited area fraction across the globe and regions of interest. Colored lines depict the globally and decadally average time series of water-limited fraction of the warm land area, averaged over all individual models.

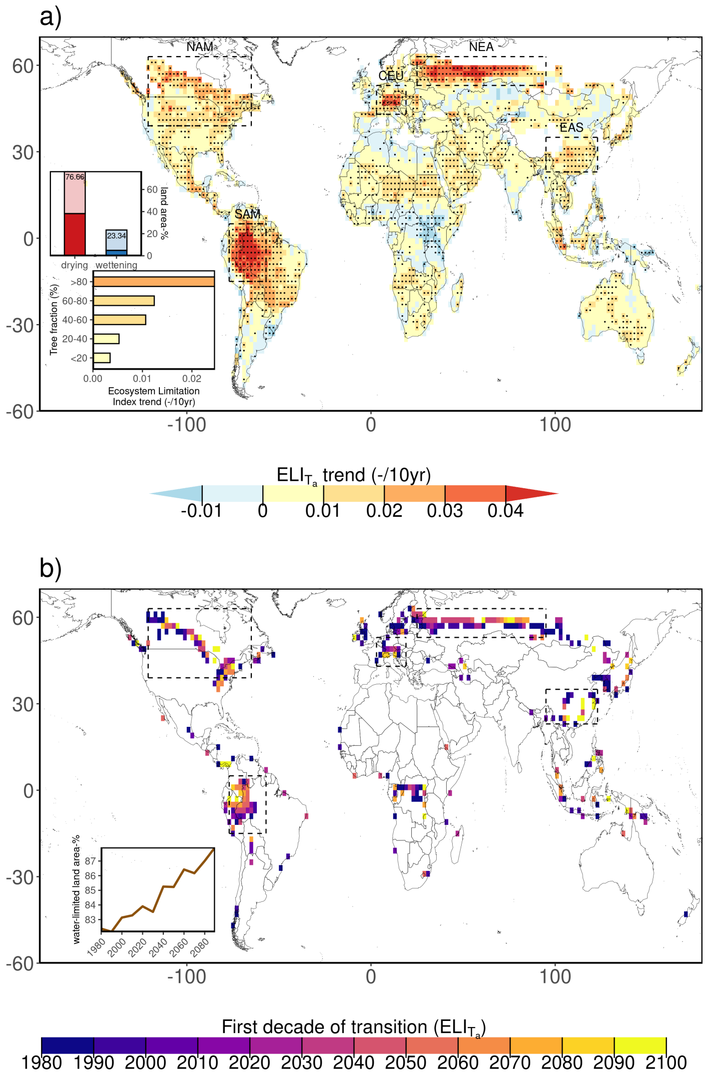

Supplementary Figure 13: Global distribution and trends of ecosystem water limitation derived with air temperature (T_a) instead of incoming shortwave radiation anomalies. a) Trend in the multi-model mean of ELI (dots indicate significance: $p < 0.05$ based on Kendall's tau statistic). The dashed boxes indicate regions of interest, which allow easier cross-comparisons with other maps. The top inset displays the fraction of the warm land area that is drying or wettening according to ELI trends ($p < 0.05$ is hued darker). The bottom inset displays area-weighted average ELI trends for regions with different tree fractions based on 6 CMIP6 models (Methods). b) Timing of regime shift from energy to water limitation as indicated by ELI values becoming positive. The inset shows the global time series of the water-limited fraction of the warm land area (Methods).

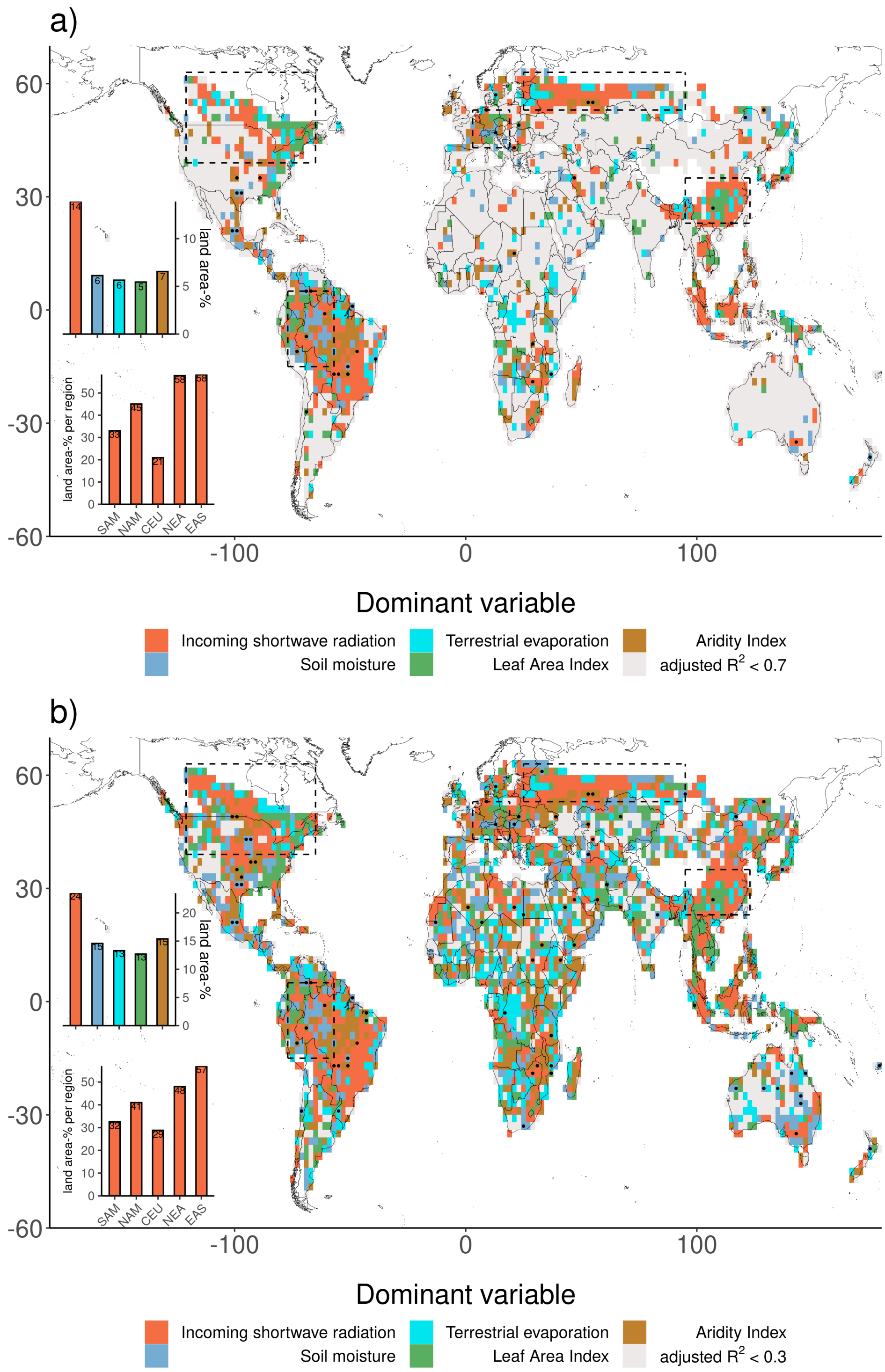

Supplementary figure 14: Attribution of ELI trends to land-atmosphere variables with different thresholds for explanatory power of the multiple linear models. Adjusted $R^2 > 0.7$ a) and adjusted $R^2 > 0.3$ b). Colors indicate the variables that best predict the decadal ELI dynamics calculated using multivariate linear regression with a set of equally well-performing models, across which the most meaningful predictor is selected (Methods). Stippling indicates grid cells where only one linear model performs well (exceeding the respective adjusted R^2 threshold) and contains only a single explanatory variable. Grey color denotes grid cells without any model with reliable performance (not exceeding the respective adjusted R^2 threshold). Inset plots indicate the total fraction of warm land area controlled by respective variables (top) and the fraction of ELI trends controlled by incoming shortwave radiation per region of interest.

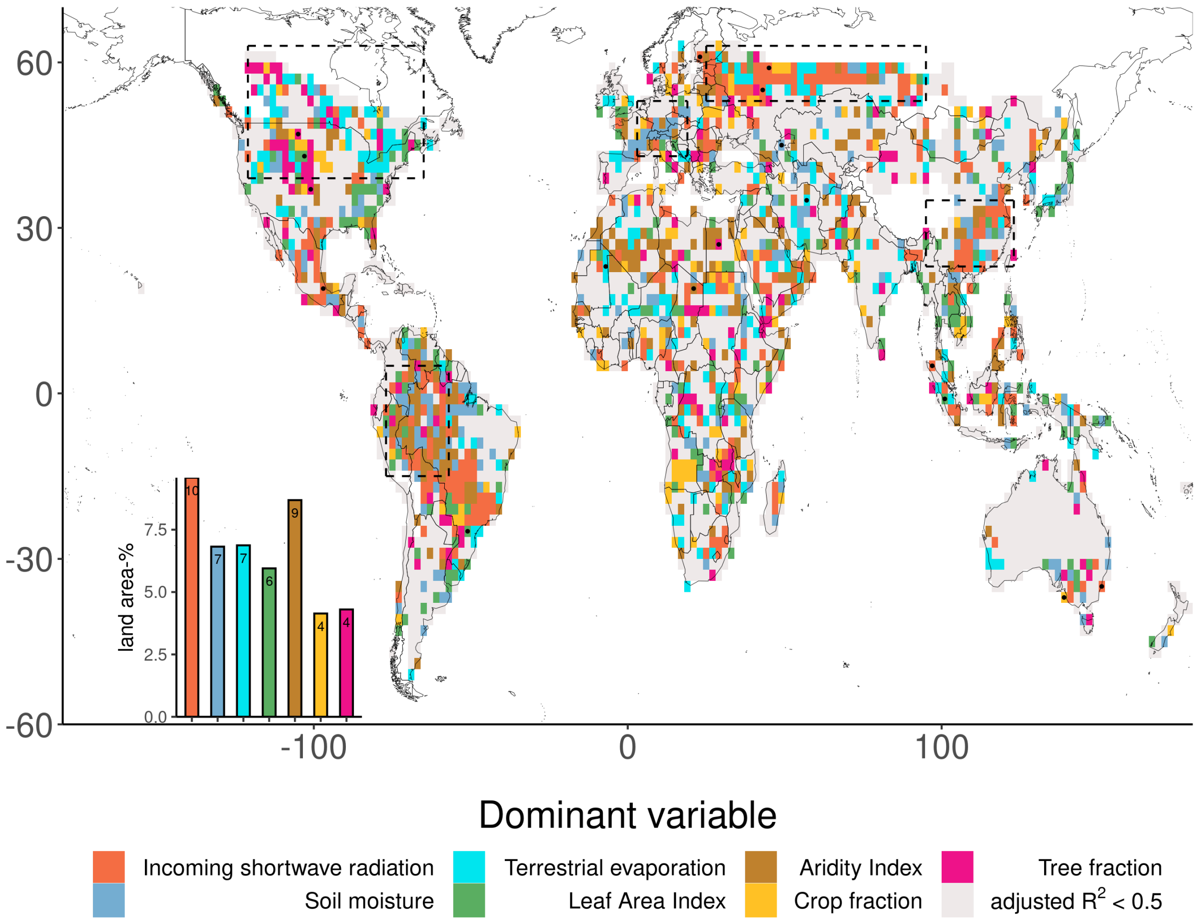

Supplementary figure 15: Attribution of ELI trends to land-atmosphere variables including proxies for land use change, crop and tree fraction (for 6 CMIP6 models only; Methods). Dots indicate that there is only one linear model that is significant (adjusted $R^2 > 0.5$) and contains only one single explanatory variable, and grey warm land area lacking any significant multivariate linear model (adjusted $R^2 < 0.5$). Inset plots indicate the total fraction of warm land area governed by respective variables.

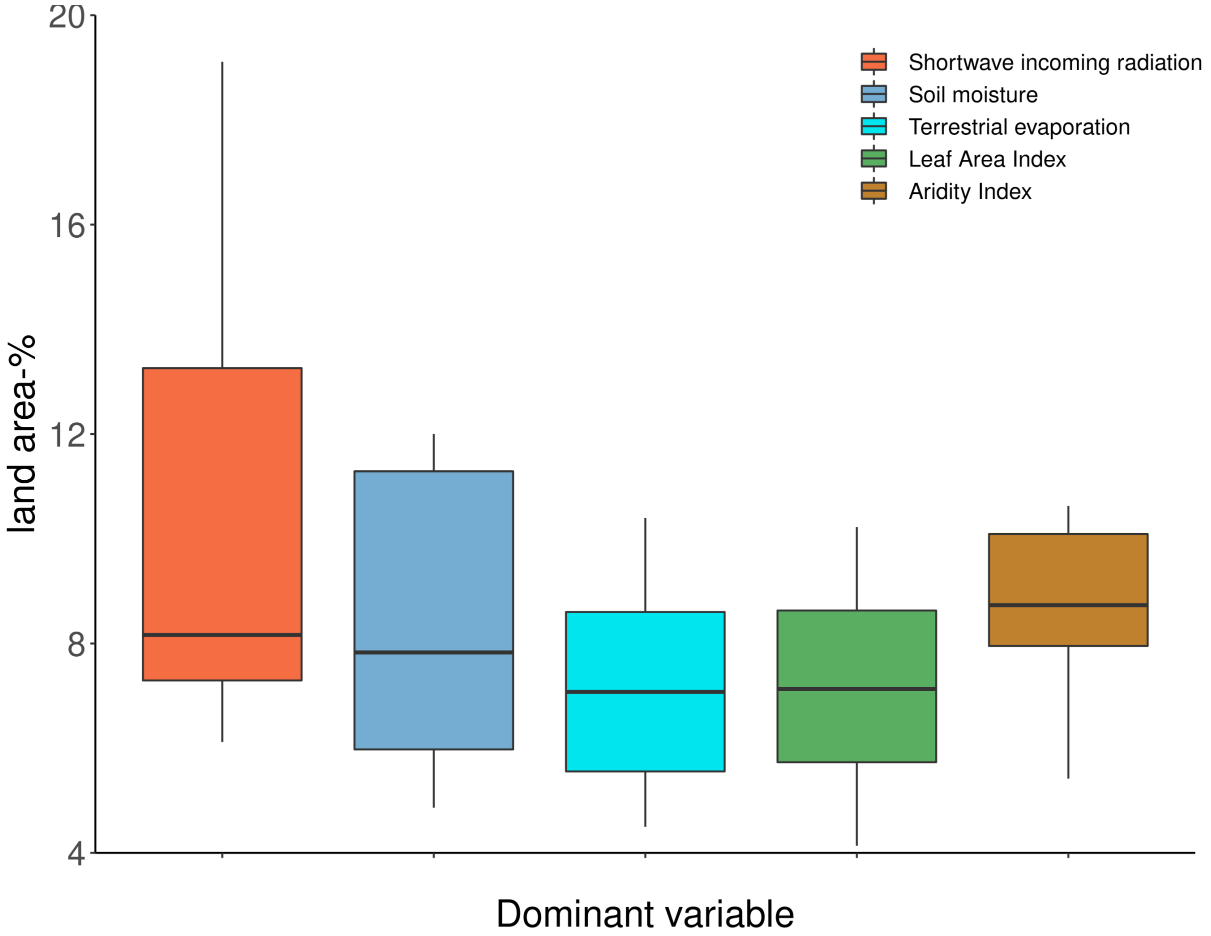

Supplementary figure 16: The importance of land-atmosphere variables per CMIP6 model. Area fraction of grid cells with adjusted R^2 > 0.5 that is governed by a respective variable. Box-and-whisker plots display the median (horizontal bar), 25^{th} and 75^{th} percentiles (hinges) and largest and smallest values that do not exceed 1.5 * of the inter-quartile range.

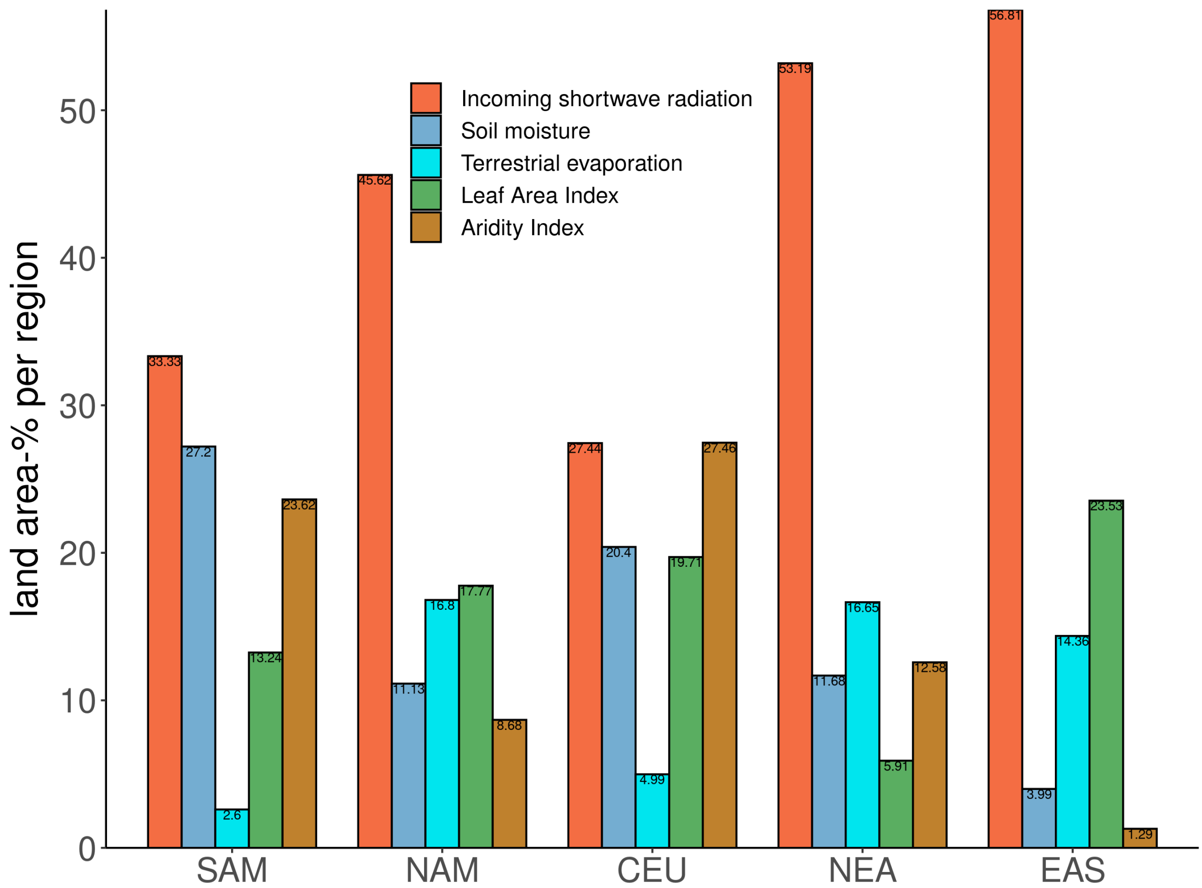

Supplementary figure 17: The importance of land-atmosphere variables per region of interest. Area fraction of grid cells within regions of interest with adjusted $R^2 > 0.5$ that is governed by a respective variable.

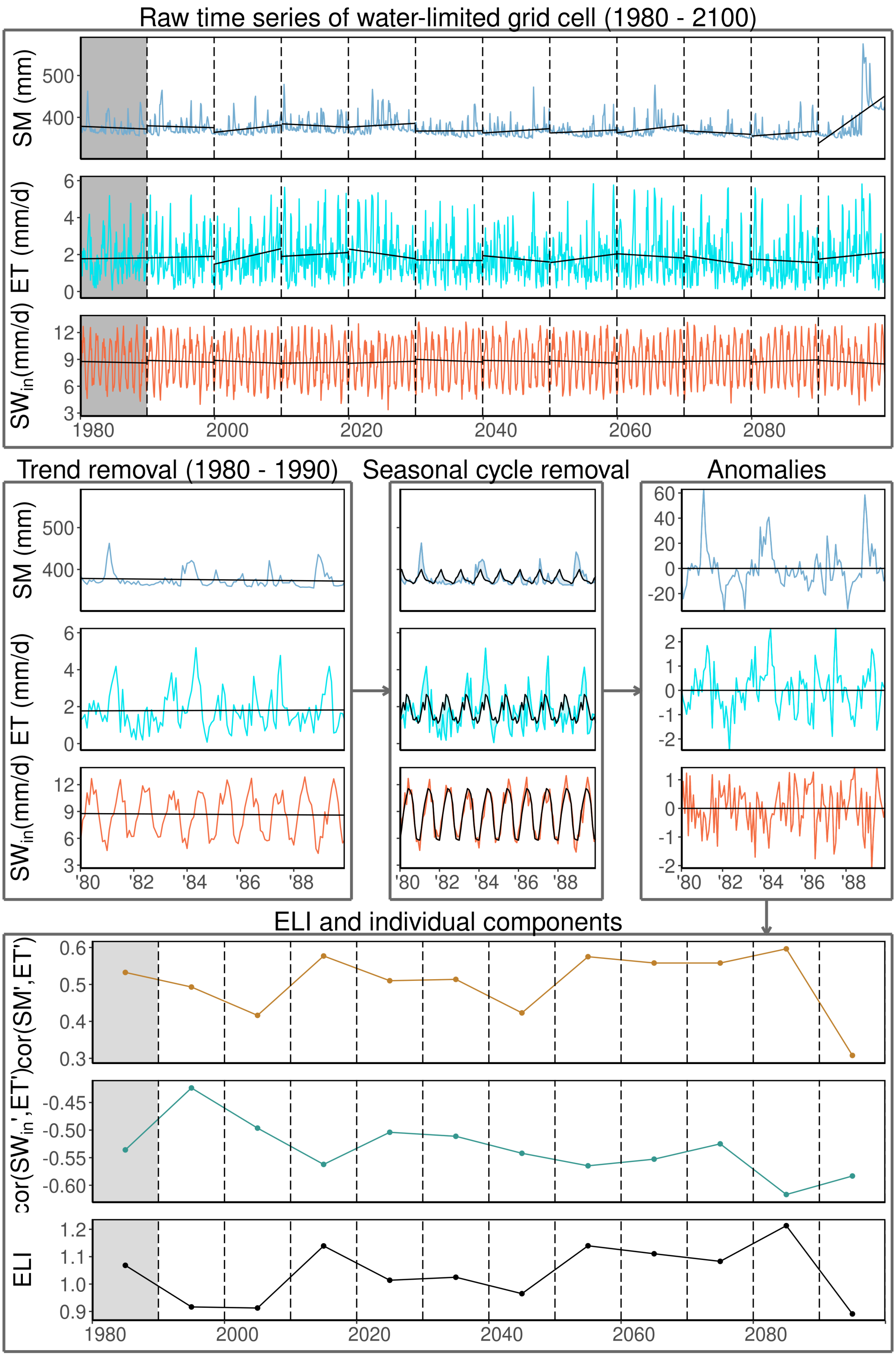

Supplementary figure 18: Illustration of procedure of computing the ELI in a water-limited example grid cell (29° N and 101° W). The colored lines in the top panel show, from top to bottom, the raw time series for the 120-year study period for soil moisture (SM), terrestrial evaporation (ET) and incoming shortwave radiation (SW_{in}). Vertical dashed lines separate the time series into decades, within which we determined the linear trends (black solid lines) we use for detrending. The grey shading indicates the decade that we use to illustrate the computation of the monthly anomalies. The left panel in the middle row shows the same as the top panel, but just for 1980-1990. The middle panel in the middle row shows the detrended time series (colored lines) imposed on the seasonal cycle (black), revealing the monthly anomalies (shaded region between colored and black lines). The colored lines in the right panel in the middle row show the anomalies, where dashed lines indicate monthly temperatures colder than 10 ˚C. Only the data in months with temperature exceeding 10 ˚C (solid lines) are used to compute the correlations that constitute the ELI. The bottom panel shows, from top to bottom, cor(SM′,ET′), cor(SW_{in}′,ET′) and the ELI. The arrows in the figure indicate step-wise computation of the ELI. All results are from the INM-CM4-8 model (Supplementary table 3).

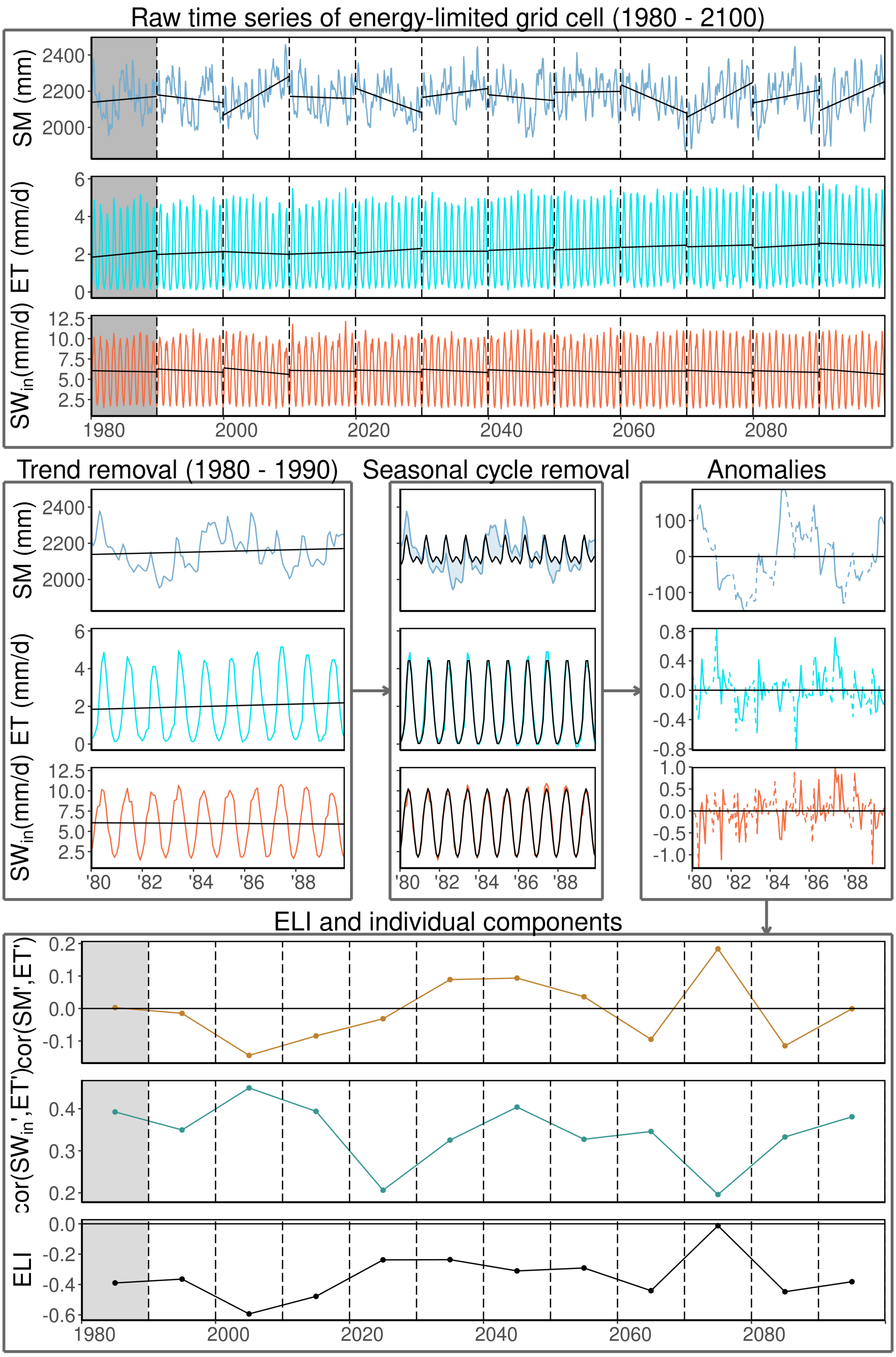

Supplementary figure 19: Similar to Supplementary Figure 17 but for an energy-limited example grid cell (49˚ N and 75˚ W).

Validation of ELI with conceptual model

Our motivation for the application of ELI to indicate water- versus energy-limited conditions was explained in the introduction. Here, we establish the ability of ELI to reflect water-limited conditions by using a conceptual soil moisture model, which is forced by the potential ET (ET_p) and precipitation, and computes actual ET, leakage from the root-zone ($Q_{leakage}$) and soil moisture (SM). The actual ET is computed as a function of ET_p and SM, as follows:

$$(1)\ ET = ET_p * \beta_{SM}$$

where the soil moisture stress function (β_{SM}) can be defined with three linear relationships:

$$(2)\ \beta_{SM} = \begin{cases} 0 & if\ SM < SM_{wilt} \\ \frac{SM - SM_{wilt}}{SM_{crit} - SM_{wilt}} & if\ SM_{wilt} < SM < SM_{crit} \\ 1 & if\ SM_{crit} < SM < SM_{sat} \end{cases}$$

where SM_{wilt} is the wilting point, SM_{crit} the critical soil moisture and SM_{sat} the soil moisture content at saturation. Soil parameters were adopted from the HTESSEL model ($SM_{wilt} = 0.171$, $SM_{crit} = 0.323$ and $SM_{sat} = 0.472$). ET_p is computed using a simplification of the Priestley-Taylor method (as previously done by Lofgren et al.[3], Milly and Dunne[4] and Maes et al.[5]):

$$(3)\ ET_p = \alpha_{MD} * R_n$$

Here, ET_p is assumed to be a fraction ($\alpha_{MD} = 0.8$) of the surface net radiation. The $Q_{leakage}$ is based on Clapp and Hornberger[6] and Buitink et al.[7]:

$$(4)\ Q_{leakage} = LSM_t - LSM_{sat}\left[\left(\frac{SM_t}{SM_{sat}}\right)^{-2b-2} + \frac{(2b+2)k_s\Delta t)}{SM_{sat}L}\right]^{-\frac{1}{2b+2}}$$

where L denotes the rooting depth (1000mm), SM_t the soil moisture content at time t, k_s is the hydraulic conductivity (50mm/d), Δt is the length of time step and b an empirical constant (taken as 5.39). Using Eqs. 1-4, the root-zone soil moisture is prognosed by solving the water balance, as follows:

$$(5)\ SM_{t+1} = SM_t + \frac{1}{L}\left(P - ET - Q_{leakage}\right)$$

where P is total precipitation. The concept of water limitation is straightforward through the implementation of the soil moisture stress function in Eq. (2) in the model, which renders this model suitable to validate the ability of ELI to reflect water limited conditions. In climate models, water limitation is more complex as it is related to several interacting processes and resulting complex soil moisture stress functions are not readily available as model output, warranting the application of a more descriptive index, such as the ELI. Here, we define an index that computes the fraction of days where water-limited conditions prevail (when SM < SM_{crit}, although it should be noted that this is just one definition of water limitation used here for illustration only).

We solve this set of equations using surface net radiation and total precipitation from ERA5 at the daily time scale at a 0.5 x 0.5 degree grid cell resolution from 1981-2016[8,9]. The fraction of days where SM < SM_{crit} is computed for every 5-year time interval. In concert, the ELI is computed as described in the Methods section. We modify this methodology by computing the ELI i) with the net radiation from ERA5 that is used as model input and the soil moisture and terrestrial evaporation directly computed by the conceptual model (Equations (1) and (4)) and ii) for every 5-year time interval to obtain a reasonable time sample, excluding data where there are fewer than 15 data points with temperatures above 10˚C.

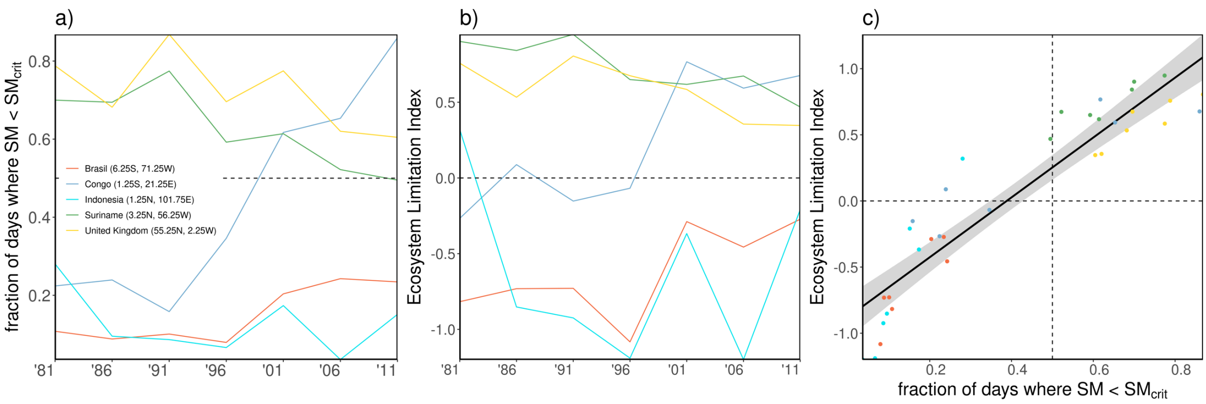

Supplementary Figure 20: Validation of the ability of ELI to reflect water-limited conditions. Time series of a) fraction of days where SM < SM_{crit} and b) ELI and c) fraction of days where SM < SM_{crit} versus ELI with data from the conceptual model (points). The solid black line in c) denotes a linear regression with a 95% confidence interval. Colors denote different grid cells, selected across the globe and different climate regimes. Conditions above and right of the dashed lines are assumed water-limited.

Time series of the fraction of days where SM < SM_{crit} and the ELI are shown in Supplementary Figure 20a and b for a number of grid cells distributed across the globe. Note that grid cells have been selected to reflect a wide range of average climate conditions; from energy- to water-limited conditions. The order of the time series in both panels are similar, suggesting comparable spatial variability between the two indices. Further, all grid cells show ample temporal variability; Whereas the magnitude of the temporal variability is not as straightforward to compare between a) and b), the sign of the changes in time of both indices match well. Also, the high correlation between ELI and the conceptual water balance estimates of water limitation shown in Supplementary Figure 20c confirms the similarity between these two indices and validates, at least for this selection of grid cells, that the ELI is able to reflect water-limited conditions.

Tables

Supplementary table 1: Conceptual typical behavior of ELI (cor(SM′,ET′) - cor(SW_{in}′,ET′)) and its individual components cor(SM′,ET′) and cor(SW_{in}′,ET′) across soil moisture regimes.

	SM < SM_{wilt}	SM_{wilt} < SM < SM_{crit}	SM > SM_{crit}

Regime	dry	water limitation	energy limitation
cor(SM′,ET′)	≈ 0	> 0	< 0 or ≈ 0
cor(SW$_{in}$′,ET′)	≈ 0	< 0 or ≈ 0	> 0
ELI	≈ 0	> 0	< 0

Supplementary table 2: Overview of signs of individual correlations of the ELI typically associated with water and energy-limited conditions, respectively. All values denote the median of model-specific area fraction of water-limited or energy-limited warm land area that satisfies the combinations; within brackets the interquartile range.

water limitation (ELI > 0)	**energy limitation (ELI < 0)**
cor(SM′,ET′) > 0 & cor(SW$_{in}$′,ET′) < 0: 84% (7)	cor(SM′,ET′) < 0 & cor(SW$_{in}$′,ET′) > 0: 58% (10)
cor(SM′,ET′) > 0 & cor(SW$_{in}$′,ET′) > 0: 15% (5)	cor(SM′,ET′) > 0 & cor(SW$_{in}$′,ET′) > 0: 40% (10)

Supplementary table 3: An overview of the CMIP6 models used in this study. For all models, variables temperature (tas), root-zone soil moisture (mrso), terrestrial evaporation (hfls), Leaf Area Index (lai), precipitation (pr) and in- and outcoming short- and longwave radiation (rlds,rsds,rlus,rsus) have been downloaded; here, all variables are abbreviated according to CMIP6 standardized names. *models that additionally provide variables evaporation from the canopy (evspsblveg) and near-surface relative humidity (hurs). **models that additionally provide variables crop fraction (cropFrac) and tree fraction (treeFrac). ***CAMS-CSM1-0 does not contain output for the year 2100, which is copied from 2099, and TaiESM1 does not contain data from December 2100, which is copied from November 2099. Dynamic vegetation reflects whether or not plant functional traits (PFT) can vary in time, responding to competition for resources. However, the resources considered in this context vary between models.

Institution	Model	Member	Version	Dynamic vegetation	Citation
National oceanic and Atmospheric Administration (NOAA), Geophysical Fluid Dynamics Laboratory (GFDL)*	GFDL-CM4	r1i1p1f1	v20180701	yes	[10–12]
Centre National de Recherches Meteorologiques (CNRM)*/**	CNRM-ESM2-1	r1i1p1f2	v20191021	no	[13–15]
Beijing Climate Center (BCC)	BCC-CSM2-MR	r1i1p1f1	v20190314	no	[16–18]
EC-Earth-Consortium*/**	EC-Earth3-Veg	r2i1p1f1	v20200226	yes	[19–21]
Met Office Hadley Centre (MOHC)*	UKESM1-0-LL	r2i1p1f2	v20190507	yes	[22–24]

Institute for Numerical Mathematics (INM)[*/**]	INM-CM4-8	r1i1p1f1	v20190603	no	[25–27]
Chinese Academy of Meteorological Sciences (CAMS)[***]	CAMS-CSM1-0	r2i1p1f1	v20190924	yes	[28–30]
National Center for Atmospheric Research (NCAR)[*/**]	CESM2	r4i1p1f1	v20200528	yes	[31–33]
Commonwealth Scientific and Industrial Research Organisation (CSIRO)[**]	ACCESS-ESM1-5	r1i1p1f1	v20191115	yes	[34–36]
Fondazione Centro Euro-Mediterraneo sui Cambiamenti (CMCC)[*/**]	CMCC-CM2-SR5	r1i1p1f1	v20200622	yes	[37–39]

Research Center for Environmental Changes (AS-RCEC)***	TaiESM1	r1i1p1f1	v20200901	no	[40–42]

Supplementary table 4: Indicates which predictors have been applied for which figures. From which models the predictors are available can be found in Table 3. *S denotes a Supplementary figure.

Predictors	Used for Figure*
Incoming shortwave radiation, soil moisture, terrestrial evaporation, Leaf Area Index, Aridity Index	4, S12-14
Crop & tree fraction	S13

References

1. Wickham, H. *et al. ggplot2: Create Elegant Data Visualisations Using the Grammar of Graphics*. (2022).
2. Bivand, R. *et al. maptools: Tools for Handling Spatial Objects*. (2022).
3. Lofgren, B. M., Hunter, T. S. & Wilbarger, J. Effects of using air temperature as a proxy for potential evapotranspiration in climate change scenarios of Great Lakes basin hydrology. *Journal of Great Lakes Research* **37**, 744–752 (2011).
4. Milly, P. C. D. & Dunne, K. A. Potential evapotranspiration and continental drying. *Nature Clim Change* **6**, 946–949 (2016).

5. Maes, W. H., Gentine, P., Verhoest, N. E. C. & Miralles, D. G. Potential evaporation at eddy-covariance sites across the globe. *Hydrology and Earth System Sciences* **23**, 925–948 (2019).
6. Clapp, R. B. & Hornberger, G. M. Empirical equations for some soil hydraulic properties. *Water Resources Research* **14**, 601–604 (1978).
7. Buitink, J., Melsen, L. A. & Teuling, A. J. Seasonal discharge response to temperature-driven changes in evaporation and snow processes in the Rhine Basin. *Earth System Dynamics* **12**, 387–400 (2021).
8. Hersbach, H. *et al.* The ERA5 global reanalysis. *Quarterly Journal of the Royal Meteorological Society* **146**, 1999–2049 (2020).
9. Hersbach, H. *et al.* ERA5 monthly averaged data on single levels from 1979 to present. (2019) doi:10.24381/CDS.F17050D7.
10. Held, I. M. *et al.* Structure and Performance of GFDL's CM4.0 Climate Model. *Journal of Advances in Modeling Earth Systems* **11**, 3691–3727 (2019).
11. Guo, H. *et al.* NOAA-GFDL GFDL-CM4 model output historical. (2018) doi:10.22033/ESGF/CMIP6.8594.
12. Guo, H. *et al.* NOAA-GFDL GFDL-CM4 model output prepared for CMIP6 ScenarioMIP. (2018) doi:10.22033/ESGF/CMIP6.9242.
13. Seferian, R. CNRM-CERFACS CNRM-ESM2-1 model output prepared for CMIP6 CMIP historical. (2018) doi:10.22033/ESGF/CMIP6.4068.
14. Séférian, R. *et al.* Evaluation of CNRM Earth System Model, CNRM-ESM2-1: Role of Earth System Processes in Present-Day and Future Climate. *Journal of Advances in Modeling Earth Systems* **11**, 4182–4227 (2019).
15. Voldoire, A. CNRM-CERFACS CNRM-ESM2-1 model output prepared for CMIP6 ScenarioMIP ssp585. (2019) doi:10.22033/ESGF/CMIP6.4226.

16. Wu, T. *et al.* The Beijing Climate Center Climate System Model (BCC-CSM): the main progress from CMIP5 to CMIP6. *Geoscientific Model Development* **12**, 1573–1600 (2019).
17. Wu, T. *et al.* BCC BCC-CSM2MR model output prepared for CMIP6 CMIP historical. (2018) doi:10.22033/ESGF/CMIP6.2948.
18. Xin, X. *et al.* BCC BCC-CSM2MR model output prepared for CMIP6 ScenarioMIP ssp370. (2019) doi:10.22033/ESGF/CMIP6.3035.
19. Consortium (EC-Earth), E.-E. EC-Earth-Consortium EC-Earth3-Veg-LR model output prepared for CMIP6 CMIP historical. (2020) doi:10.22033/ESGF/CMIP6.4707.
20. Consortium (EC-Earth), E.-E. EC-Earth-Consortium EC-Earth3-Veg model output prepared for CMIP6 ScenarioMIP. (2019) doi:10.22033/ESGF/CMIP6.727.
21. Döscher, R. *et al.* The EC-Earth3 Earth System Model for the Climate Model Intercomparison Project 6. *Geoscientific Model Development Discussions* 1–90 (2021) doi:10.5194/gmd-2020-446.
22. Good, P. *et al.* MOHC UKESM1.0-LL model output prepared for CMIP6 ScenarioMIP. (2019) doi:10.22033/ESGF/CMIP6.1567.
23. Tang, Y. *et al.* MOHC UKESM1.0-LL model output prepared for CMIP6 CMIP historical. (2019) doi:10.22033/ESGF/CMIP6.6113.
24. Sellar, A. A. *et al.* UKESM1: Description and Evaluation of the U.K. Earth System Model. *Journal of Advances in Modeling Earth Systems* **11**, 4513–4558 (2019).
25. Volodin, E. M. *et al.* Simulation of the modern climate using the INM-CM48 climate model. *Russian Journal of Numerical Analysis and Mathematical Modelling* **33**, 367–374 (2018).
26. Volodin, E. *et al.* INM INM-CM4-8 model output prepared for CMIP6 CMIP historical. (2019) doi:10.22033/ESGF/CMIP6.5069.

27. Volodin, E. *et al.* INM INM-CM4-8 model output prepared for CMIP6 ScenarioMIP. (2019) doi:10.22033/ESGF/CMIP6.12321.

28. Rong, X. CAMS CAMS_CSM1.0 model output prepared for CMIP6 CMIP historical. (2019) doi:10.22033/ESGF/CMIP6.9754.

29. Rong, X. CAMS CAMS-CSM1.0 model output prepared for CMIP6 ScenarioMIP. (2019) doi:10.22033/ESGF/CMIP6.11004.

30. Rong, X.-Y. *et al.* Introduction of CAMS-CSM model and its participation in CMIP6. *Advances in Climate Change Research* **15**, 540 (2019).

31. Danabasoglu, G. NCAR CESM2 model output prepared for CMIP6 CMIP historical. (2019) doi:10.22033/ESGF/CMIP6.7627.

32. Danabasoglu, G. NCAR CESM2 model output prepared for CMIP6 ScenarioMIP ssp585. (2019) doi:10.22033/ESGF/CMIP6.7768.

33. Danabasoglu, G. *et al.* The Community Earth System Model Version 2 (CESM2). *Journal of Advances in Modeling Earth Systems* **12**, e2019MS001916 (2020).

34. Ziehn, T. *et al.* The Australian Earth System Model: ACCESS-ESM1.5. *JSHESS* **70**, 193–214 (2020).

35. Ziehn, T. *et al.* CSIRO ACCESS-ESM1.5 model output prepared for CMIP6 CMIP historical. (2019) doi:10.22033/ESGF/CMIP6.4272.

36. Ziehn, T. *et al.* CSIRO ACCESS-ESM1.5 model output prepared for CMIP6 ScenarioMIP ssp585. (2019) doi:10.22033/ESGF/CMIP6.4333.

37. Cherchi, A. *et al.* Global Mean Climate and Main Patterns of Variability in the CMCC-CM2 Coupled Model. *Journal of Advances in Modeling Earth Systems* **11**, 185–209 (2019).

38. Lovato, T. & Peano, D. CMCC CMCC-CM2-SR5 model output prepared for CMIP6 CMIP historical. (2020) doi:10.22033/ESGF/CMIP6.3825.

39. Lovato, T. & Peano, D. CMCC CMCC-CM2-SR5 model output prepared for CMIP6 ScenarioMIP. (2020) doi:10.22033/ESGF/CMIP6.1365.

40. Lee, W.-L. & Liang, H.-C. AS-RCEC TaiESM1.0 model output prepared for CMIP6 CMIP historical. (2020) doi:10.22033/ESGF/CMIP6.9755.

41. Lee, W.-L. & Liang, H.-C. AS-RCEC TaiESM1.0 model output prepared for CMIP6 CMIP. (2019) doi:10.22033/ESGF/CMIP6.9684.

42. Lee, W.-L. *et al.* Taiwan Earth System Model Version 1: description and evaluation of mean state. *Geoscientific Model Development* **13**, 3887–3904 (2020).